

# Stochastic finite element framework for simultaneous estimation of cardiac kinematic functions and material parameters

Pengcheng Shi<sup>a,\*</sup>, Huafeng Liu<sup>a,b</sup>

<sup>a</sup>Biomedical Research Laboratory, Department of Electrical and Electronic Engineering, Hong Kong University of Science and Technology, Clear Water Bay, Kowloon, Hong Kong, Hong Kong

<sup>b</sup>State Key Laboratory of Modern Optical Instrumentation, Zhejiang University, Hangzhou 310027, China

## Abstract

A stochastic finite element framework is presented for the simultaneous estimation of the cardiac kinematic functions and material model parameters from periodic medical image sequences. While existing biomechanics studies of the myocardial material constitutive laws have assumed known tissue kinematic measurements, and image analysis efforts on cardiac kinematic functions have relied on fixed constraining models of mathematical or mechanical nature, we illustrate through synthetic data that a probabilistic joint estimation strategy is needed to achieve more robust and accurate analysis of the kinematic functions and material parameters at the same time. For a particular a priori constraining material model with uncertain subject-dependent parameters and a posteriori noisy imaging based observations, our strategy combines the stochastic differential equations of the myocardial dynamics with the finite element method, and the material parameters and the imaging data are treated as random variables with known prior statistics. After the conversion to state space representation, the extended Kalman filtering procedures are adopted to linearize the equations and to provide the joint estimates in an approximate optimal sense. The estimation bias and convergence issues are addressed, and we conclude experimentally that it is possible to adopt this biomechanical model based multiframe estimation approach to achieve converged estimates because of the periodic nature of the cardiac dynamics. The effort is validated using synthetic data sequence with known kinematics and material parameters. Further, under linear elastic material model, estimation results using canine magnetic resonance phase contrast image sequences are presented, which are in very good agreement with histological tissue staining results, the current gold standards.

© 2003 Elsevier B.V. All rights reserved.

**Keywords:** Cardiac motion analysis; Myocardium material characterization; Stochastic finite element method; Simultaneous estimation; Multiframe estimation

## 1. Introduction

Quantitative and noninvasive estimation of cardiac material properties and regional kinematic functions has significant clinical and physiological implications. In abstract terms, the dynamic system for the biomechanics-based cardiac kinematics and material analysis can be stated as follows:

$$\Phi(q, u(q)) = \Pi(u(q)), \quad (1)$$

with constraining material model parameters  $q$ , kinematics states  $u(q)$ , system differential operators  $\Phi$ , and loads  $\Pi$ . The goals are then to use the noisy and incomplete observations on the kinematics states to either determine

the best model parameters  $q^*$  in some admissible set so that the solution to Eq. (1) for  $q = q^*$  best describes the data (the determination of material parameters in biomechanics research) (Hunter and Smaill, 1989; Moulton et al., 1995), and/or to determine the best state vectors  $u^*$  in some feasible physical space so that the solution to Eq. (1) for  $u = u^*$  best fits the data under the constraints of the material model (the determination of kinematic parameters in image analysis) (Papademetris et al., 2002; Shi et al., 1999).

### 1.1. Cardiac motion analysis

Acute and chronic myocardial ischemia can be identified and localized through the detection of morphological and kinematic abnormalities of the left ventricle (LV) (Lipton et al., 2002). Accordingly, there have been abundant

\*Corresponding author. Tel.: +852-2358-8529; fax: +852-2335-0194.  
E-mail address: eeship@ust.hk (P. Shi).

efforts devoted to cardiac motion and deformation recovery from medical image sequences (Duncan and Ayache, 2000; Frangi et al., 2001, 2002). Imaging-derived sparse salient features of the myocardium have been used to establish correspondences between cardiac image frames, including the use of implanted physical markers (McCulloch, 1995; Waldman et al., 1985), crossings of magnetic resonance imaging (MRI) tag lines (Amini et al., 2001; Denney, 1999; Guttman et al., 1994; Kerwin and Prince, 1999b; Kumar and Goldgof, 1994; Moore et al., 1992; Osman et al., 2000; Young et al., 1995), geometrically significant shape landmarks (Amini and Duncan, 1992; Kambhamettu and Goldgof, 1994; McEachen and Duncan, 1997; Shi et al., 2000), and integration of MRI phase contrast velocity (Constable et al., 1994; Meyer et al., 1996; Pelc et al., 1995; Zhu et al., 1997). Normally, however, the locations and thus the displacements of these detected landmarks are corrupted by noises, and the recovery of the dense field motion and deformation parameters for the entire myocardium from this sparse set of noisy landmark displacements is an ill-posed problem and needs additional constraints to obtain a unique solution in some optimal sense. Various strategies have been proposed with varying degree of success, including notable examples of mathematically motivated regularization (McEachen and Duncan, 1997; Shi et al., 2000; Young et al., 1995), finite element method (FEM) based modal analysis (Benayoun and Ayache, 1998; Sclaroff and Pentland, 1995), deformable superquadrics (Park et al., 1996), spatiotemporal B-Spline (Huang et al., 1999), Fisher estimator with smoothness and incompressibility assumptions (Denney and Prince, 1995), and continuum biomechanics based energy minimization (Papademetris et al., 2002; Papademetris et al., 2001; Shi et al., 1999).

Because of the periodic nature of the heart motion, the importance of adopting multiframe analysis is well recognized yet rarely addressed in a systematic fashion (McEachen et al., 2000). While many of the aforementioned efforts deal with frame-to-frame motion only, several attempts do try to track the motion over the entire cardiac cycle using explicit temporal modeling and thus are of particular relevance to our work. Assuming elliptic trajectories for the cardiac tissue elements, a Kalman filter framework is constructed to estimate two-dimensional (2D) left ventricular deformation from spline-regularized MRI phase contrast velocity fields that are constrained by segmented endocardial and epicardial contours (Meyer et al., 1996). MR phase contrast images are also studied using the Fourier tracking method in frequency domain (Pelc et al., 1995; Zhu et al., 1997), where the motion trajectories are computed as composed of Fourier harmonics and the tracking results are then fitted into a deformation model. This strategy is later extended to the dynamic mesh model that expresses complex object motion/deformation in space and time with time-varying finite elements and provides a flexible tradeoff between analysis accuracy and reproducibility with controllable

built-in spatiotemporal smoothing (Zhu and Pelc, 1999). In (Kerwin and Prince, 1999a), the stochastic spatial interpolator of universal kriging is combined with the stochastic temporal filter, the well-known Kalman filter, to form a state equation representation, the so-called *kriging update model*, that permits a recursive solution for estimating a function in time and space. And in (McEachen et al., 2000), a recursive least-square algorithm based on an adaptive transversal filter is developed to facilitate the integration of models for periodicity and proximal smoothness as appropriate using a contour-based description of the myocardial boundaries, where the multiframe temporal models are based on a sum of sinusoids, and a set of correspondences between contours and an associated set of correspondence quality measures comprise the input to the system.

Conjugate to the efforts from the biomechanics community, all image analysis works are based on the premise that mechanical or other constraining models are known as prior information, and the issue is to use these models along with the imaging data to estimate the kinematics parameters in some optimal sense. The selection of an appropriate model with proper parameters thus largely determines the quality of the analysis results. In practical situations, especially for pathological data sets, however, it is almost impossible to have the *exact* patient-dependent model information a priori.

### 1.2. Myocardium material characterization

More fundamentally in terms of physiology, it is recognized that alterations in myocardial fiber structure and material elasticity are related to various cardiac pathologies (Wickline et al., 1992). Assuming that the kinematic measurements of the heart tissues are known from implanted markers or imaging techniques, there have been many efforts focusing on describing myocardial material characteristics from the biomechanics community (Glass et al., 1991), and more recently, from the medical imaging community (Creswell et al., 1994; Hu et al., 2002; Muthupilla et al., 1995).

In traditional biomechanics efforts of estimating material constitutive laws, regional finite deformations at isolated locations are determined by experimental means. For intact state, the distributions of stress are determined by the three-dimensional (3D) structure of the ventricular walls, the boundary conditions imposed by cavity and pericardial pressures and the fibrous valve ring at the base of the ventricle, and the mechanical properties of the myofiber and its inter-connection with collagen in the relaxed and actively contracting states (Guccione et al., 1991; Hunter and Smaill, 1989). Mathematical reasoning is then used to arrive at some suitable constitutive relationships. A key drawback of these studies is their limited clinical usefulness because of the difficulty to make patient-specific assessment of the entire heart in a noninvasive manner.

MRI tagging technique has been used for the noninva-

sive in vivo study of the mechanics of the entire heart. In (Creswell et al., 1994) and (Moulton et al., 1995), a two-dimensional early diastolic finite element (FE) mesh is constructed with loading parameters measured during MR imaging. FE solution is performed using small-strain, small-displacement theory, and corresponding regional wall strains are computed independently using MR tagging data. Two unknown parameters are then determined for an exponential strain energy function that maximizes the agreement between the observed (from MR tagging) and the predicted (from FE analysis) regional wall strains. Recently, an expectation maximization strategy is proposed to estimate the stiffness matrix and the active force from sparse tagging data in the maximum likelihood sense (Hu et al., 2002). As the case of traditional biomechanics strategies, the kinematics in these efforts is assumed known from MR tagging, and the goal is to use these kinematic parameters to estimate the material parameters. Unfortunately, it is well recognized that the recovery of kinematics from MR tagging is not a solved problem yet, and constraining models of mechanical nature may be needed for the kinematics recovery in the first place (Frangi et al., 2001).

More recently, magnetic resonance elastography (MRE) techniques have been developed to provide quantitative images of soft tissue material stiffness by processing the displacements resulting from actuating the tissues and using MR imaging techniques to measure the tissue displacements (Manduca et al., 2001; Muthupilla et al., 1995). While very promising in providing in vivo material parameters directly, this technology is still under early development and so far there have been only very limited experiments on shallow or exposed static soft tissues such as breast and brain (Manduca et al., 2001). No possibility for in vivo MRE of myocardium is at sight.

### 1.3. Joint estimation of cardiac motion and material properties

In this paper, we present a stochastic finite element framework for the simultaneous joint estimation of the cardiac kinematics (displacement and strain) and material properties (parameters of constitutive laws) from periodic medical image sequence. Given the uncertainty of the material properties for a particular patient and the noisy nature of the imaging data, we believe that a probabilistic joint estimation strategy is needed to achieve robust and optimal estimates for a particular a priori constraining model with uncertain parameters and a posteriori noisy observations on kinematics. The material parameters and the imaging/image-derived data are treated as random variables with known prior statistics in the dynamic system and measurement equations of the heart. In our current implementation, the extended Kalman filter (EKF) procedures are adopted to linearize the augmented state representation of the cardiac dynamics and to provide the joint estimates in the minimum-mean-square-error sense.

Because of the periodic nature of the cardiac behavior, we show experimentally that it is possible to adopt this physical model based statistical estimation approach, which is not restricted to any particular imaging data, to achieve converged estimates.

Our stochastic finite element method based framework has made contributions in several important aspects. Coupling the stochastic modeling of the myocardial behavior with the finite element method, we can now deal with noisy imaging data and uncertain constraining material parameters in a coordinated effort. We believe that this is the first attempt in image analysis that incorporates uncertain constraining models in the ill-posed recovery problems. The biomechanically constrained state space representation, along with the periodic nature of cardiac image sequence, makes it possible to jointly estimate the cardiac kinematics and material properties at the same time by adopting an extended Kalman filter strategy and by cyclically feeding the updated imaging data constraints until convergence. In addition to experiments using synthetic data, very promising results using canine MR images are presented, which are in very good agreement with TTC-stained post mortem tissue, the histological gold standard.

## 2. Methodology

### 2.1. Biomechanical model of the myocardium

In order to construct a realistic, yet computationally feasible, analysis framework using the imaging data and other available physical measurements such as intra-ventricular pressure, the structure and material of the left ventricle should be properly modeled. In general, the heart is a non-rigid object that deforms over time and has very complicated material properties in terms of the underlying constitutive laws (Glass et al., 1991). For computational simplicity, in our current 2D implementation, we adopt the linear isotropic continuum material for the myocardium, where the stress  $\sigma$  and strain  $\varepsilon$  relationship obeys the Hooke's law,

$$\sigma = S\varepsilon, \quad (2)$$

and  $S$  is the strain-stress matrix.

For two-dimensional case presented in this paper, assuming the displacement along the  $x$ - and  $y$ -axis of a point to be  $u(x,y)$  and  $v(x,y)$ , respectively, the infinitesimal strain tensor  $\varepsilon$  of the point can be expressed as

$$\varepsilon = \begin{bmatrix} \frac{\partial u}{\partial x} & \frac{\partial v}{\partial y} \\ \frac{\partial u}{\partial y} + \frac{\partial v}{\partial x} \end{bmatrix}. \quad (3)$$

Under plane strain condition, matrix  $S$  can be derived to be

$$S = \frac{E}{(1+\nu)(1-2\nu)} \begin{bmatrix} 1-\nu & \nu & 0 \\ \nu & 1-\nu & 0 \\ 0 & 0 & \frac{1-2\nu}{2} \end{bmatrix}. \quad (4)$$

Here, the Young's modulus  $E$  and the Poisson's ratio  $\nu$  are two material-specific parameters which will be estimated in our framework. It is quite clear from these relationships that the internal stress caused by the deformation is a function of the displacement vector and the material parameters.

Ideally, the problem should be tackled in three-dimension to avoid the through-plane motion effect. Further, the more realistic model, the transversely isotropic material (Glass et al., 1991) which accounts for the preferential stiffness in the myofiber directions (the fiber stiffness is about 1.5–3 times greater than the cross-fiber stiffness in normal cases), can be easily adopted for 3D analysis if the myofiber structure is available from the fiber model (Nielsen et al., 1991) or from diffusion tensor magnetic resonance images (DTMRI) (Geerts et al., 2002). A simplified version of this model was used for frame-to-frame cardiac motion recovery in (Papademetris et al., 2002). In the current paper, we use the simple linear model to illustrate the basic ideas and rationales of a novel joint estimation strategy.

## 2.2. Stochastic finite element method

In biomechanics studies and image analysis of the left ventricle, the deterministic finite element method has provided an efficient representation of the complex LV geometry and a convenient and effective computational framework (Benayoun and Ayache, 1998; Creswell et al., 1994; Guccione et al., 1991; Hunter and Smaill, 1989; Moulton et al., 1995; Papademetris et al., 2002, 2001; Park et al., 1996; Sclaroff and Pentland, 1995; Shi et al., 1999; Young et al., 1995). It does not, however, have the capability to consider situations where material model parameters, external loads, and kinematic observations should be characterized as stochastic processes. Since the imaging and imaging-derived observations are usually corrupted by noises of various nature, and the material parameters vary from one subject to another, especially for pathological situations, it is thus necessary to adopt a strategy which can account for the main sources of uncertainty in the dynamic analysis of the LV.

The stochastic finite element method (SFEM) has been used for structural dynamics analysis in probabilistic frameworks (Contreras, 1980; Klieber and Tran, 1992; Liu et al., 1986). In SFEM, structural material properties are described by random fields, possibly with known prior statistics, and the observations and loads are corrupted by noises. This way, stochastic differential or difference equations are combined with the finite element method to

study the dynamic structures with uncertainty in their structure parameters and measurements. In the analysis of left ventricle, this framework, based on Ito's calculus from a Bayesian point of view (Ikeda et al., 1996), can be adopted to give optimal estimates of the LV kinematics state and myocardial material parameters for a particular a priori mechanical model and a posteriori periodic image sequence.

In our 2D implementation, a Delaunay triangulated finite element mesh is constructed at the first image frame at end diastole (ED), bounded by automatically segmented endocardium and epicardium borders using a velocity constrained front propagation strategy (Wong et al., 2002). An isoparametric formulation defined in a natural coordinate system is used, where, for tri-nodal linear element, the basis functions are linear functions of the nodal coordinates (Bathe and Wilson, 1976). Assuming that the material parameters  $E$  and  $\nu$  are temporally constant throughout the cardiac cycle but are spatially varying, we arrive at the following system dynamics equation for the left ventricle:

$$M\ddot{U} + C\dot{U} + KU = R, \quad (5)$$

where  $M$ ,  $C$  and  $K$  are the mass, damping and stiffness matrices,  $R$  is the load vector, and  $U$  is the displacement vector. Because the myocardium density is generally considered to be uniform,  $M$  is a known function of the material density and is temporally and spatially constant.  $K$  is a function of the material constitutive law, and is related to the material-specific Young's modulus and Poisson's ratio, which may vary temporally and spatially. In our framework, these two local material parameters are treated as random variables with known a priori statistics, and will be estimated along with the motion parameters.<sup>1</sup> The damping matrix  $C$  is frequency dependent, and we assume small proportional Rayleigh damping with  $C = \alpha M + \beta K$  in our implementation (Cook, 1995). Eq. (5) is thus a stochastic differential equation in nature per Ito's calculus (Ikeda et al., 1996).

We want to point out that we intend to use this framework to enforce certain real physical constraints related to known cardiac pressures. Conceptually, it is important to note that while the finite element mesh provides the basis for approximating a continuous spatial model of physical nature, the dynamic equation also provides the basis of an appropriate temporal model for the matching and predicting of image frames.

## 2.3. State space representation

Since we have employed the linear material model, the dynamics equation (Eq. (5)) can be transformed into a

<sup>1</sup>Please note that currently we do not consider the temporal dependency of the material parameters.

state-space representation of a continuous-time linear stochastic system, typically seen in control and estimation literature (Glad and Ljung, 2000). Let the kinematic state vector  $x(t)$  and the material parameter vector  $\theta$  be

$$x(t) = \begin{bmatrix} U(t) \\ \dot{U}(t) \end{bmatrix}, \quad (6)$$

$$\theta = \begin{bmatrix} E \\ \nu \end{bmatrix}, \quad (7)$$

the state space form of Eq. (5) becomes

$$\dot{x}(t) = A_c(\theta)x(t) + B_c w(t), \quad (8)$$

where the system matrices  $A_c$  and  $B_c$ , and the control (input) term  $w$  are derived as

$$A_c = \begin{bmatrix} 0 & I \\ -M^{-1}K & -M^{-1}C \end{bmatrix}, \quad (9)$$

$$B_c = \begin{bmatrix} 0 & 0 \\ 0 & M^{-1} \end{bmatrix}, \quad (10)$$

$$w(t) = \begin{bmatrix} 0 \\ R(t) \end{bmatrix}. \quad (11)$$

Obviously,  $A_c$  and  $B_c$  relate to the material properties of the myocardial model, and  $w$  enforces the external loads.

An associated measurement equation, which describes the observations provided by the imaging or imaging-derived data  $y(t)$ , can be expressed in the form

$$y(t) = Dx(t) + e(t), \quad (12)$$

where  $D$  is a known measurement matrix designed by the user, and  $e(t)$  is the *measurement noise* which is assumed to be additive, zero mean and white ( $E[e(t)] = 0$ ,  $E[e(t)e(s)'] = R_e(t)\delta_{ts}$ ). In our case, the imaging data gives the displacement and velocity information, the same type of measures as the state vector  $x$ . The  $D$  matrix is  $N \times M$ , with  $M$  the total number of data constraints (displacement and velocity) and  $N$  the dimension of the state vector  $x$ , and is constructed from

$$D = \begin{bmatrix} D_U \\ D_{\dot{U}} \end{bmatrix}, \quad (13)$$

where  $D_U$  and  $D_{\dot{U}}$  relate to the displacement and velocity data, respectively.

In the image-based analysis of left ventricle, Eqs. (8) and (12) represent a continuous-time system with discrete-time measurements, or a so-called sampled data system. The input term  $w$ , available from pressure measurements or computed from the system equation using the initial and boundary conditions, is piecewise constant over the imaging sampling interval  $T$ . Implicitly assuming hidden Markov model for the state equations, we discretize Eq. (8) and arrive at (Bar-Shalom et al., 2001; Glad and Ljung, 2000)

$$x((k+1)T) = Ax(kT) + Bw(kT), \quad (14)$$

where

$$A = e^{A_c T}, \quad (15)$$

$$B = A_c^{-1}(e^{A_c T} - I)B_c. \quad (16)$$

Eq. (14) describes the relationship between the current state  $x(k+1)$  and the previous state  $x(k)$  and input  $w(k)$ , and matrices  $A$  and  $B$  can be computed using Pade approximation (Golub and Van Loan, 1983).

In more general form, the continuous-time system with discrete-time measurements, including the additive, zero-mean, white *process noise*  $v(t)$ , ( $E[v(t)] = 0$ ,  $E[v(t)v(s)'] = Q_v(t)\delta_{ts}$ ), independent of  $e(t)$ , can be converted to the discrete-time state equation

$$x(t+1) = A(\theta)x(t) + B(\theta)w(t) + v(t). \quad (17)$$

Once again, this equation implies that the state vector is a Markov sequence (Bar-Shalom et al., 2001).

#### 2.4. Augmented state space representation

The myocardial dynamics and observations are now represented by the dynamic system of Eqs. (17) and (12). This representation provides a natural framework for the biomechanics study of myocardium material constitutive laws with observations/measurements on the kinematic states, and for the physically motivated image analysis of cardiac kinematic properties with assumed biomechanical constraining models. In practice, however, neither the kinematics data nor the model parameters are precisely known. With the SFEM framework where the data and the model parameters are treated as random variables, possibly with known or assumed prior distributions, we now are able to determine the best estimates of the spatial distributions of the material parameters and the spatial-temporal kinematics parameters simultaneously.

In order to perform the joint estimation, the *unknown* state vector  $x$  is augmented by the *unknown* material parameter vector  $\theta$  to form the new state vector  $z = [x \ \theta]^T$ . Accordingly, Eq. (17) is converted to the new augmented state equation

$$z(t+1) = f(z(t), w(t)) + v_s(t), \quad (18)$$

with

$$f(z(t), w(t)) = \begin{bmatrix} A(\theta)x(t) + B(\theta)w(t) \\ \theta \end{bmatrix}, \quad (19)$$

$$v_s(t) = \begin{bmatrix} v(t) \\ 0 \end{bmatrix}. \quad (20)$$

In a similar fashion, the new augmented measurement equation is derived from Eq. (12):

$$y(t) = h(z(t)) + e_o(t), \quad (21)$$

with

$$h(z(t)) = [D \ 0] \begin{bmatrix} x(t) \\ \theta(t) \end{bmatrix}, \quad (22)$$

$$e_o(t) = \begin{bmatrix} e(t) \\ 0 \end{bmatrix}. \quad (23)$$

Since we have assumed known Gaussian process and measurement noises, the augmented noises are also Gaussian with distributions

$$v_s(t) \sim N(0, Q_s), \quad \text{where} \quad Q_s = \begin{bmatrix} Q_v & 0 \\ 0 & 0 \end{bmatrix}, \quad (24)$$

$$e_o(t) \sim N(0, R_o), \quad \text{where} \quad R_o = \begin{bmatrix} R_e \\ 0 \end{bmatrix}. \quad (25)$$

### 2.5. Extended Kalman filter for joint state and parameter identification

The joint state and parameter estimation problem can now be understood as a state estimation problem for the nonlinear system represented by Eqs. (18) and (21). This form of formulation leads to a solution of the filtering problem using the extended Kalman filter (EKF) framework, which is based on the linearization of the augmented state equations at each time step. A recursive procedure with natural block structure can be used to perform the joint state (kinematics) and parameter (material) estimation, and a general analysis of the algorithm convergence can be found in (Ljung, 1979).

Like a Taylor series, we can linearize the equations around the current estimates using the partial derivative of the process and measurement functions to compute the estimates even in the face of non-linear relationships. The operation of the EKF is the same one as the linear Kalman filter, which adopts a form of feedback control in estimation: the filter estimates the process state at some time and then obtains feedback in the form of measurements. As such, the equations for the EKF iterations fall into two groups: time update equations and measurement update equations. The time update equations are responsible for projecting forward the current state and error covariance estimates to obtain the a priori estimates for the next time step, while the measurement update equations are responsible for the feedback with the a posteriori data.

Initializing the EKF filter with  $\hat{z}(0) = \hat{z}_0$  and  $P(0) = \Sigma_0$ , the augmented state estimates and their error covariance matrices are computed sequentially in the following iterative fashion:

- (1) Project the state from  $t-1$  to  $t$ :

$$\hat{z}^-(t) = f(\hat{z}(t-1), w(t)). \quad (26)$$

- (2) Project the error covariance from  $t-1$  to  $t$ :

$$P^-(t) = F_t P(t-1) F_t^T + Q_s. \quad (27)$$

- (3) Compute the Kalman gain at  $t$ :

$$G(t) = P^-(t) H^T (H P^-(t) H^T + R_o)^{-1}. \quad (28)$$

- (4) Update the estimate with the measurement at  $t$ :

$$\hat{z}(t) = \hat{z}^-(t) + G(t)(z(t) - h(\hat{z}^-(t))). \quad (29)$$

- (5) Update the error covariance at  $t$ :

$$P(t) = (I - G(t)H)P^-(t). \quad (30)$$

- (6) Repeat steps (1)–(5) until convergence.

The needed quantities for Eqs. (26)–(30) are defined by

$$F_t = \frac{\partial}{\partial z} f(z(t), w(t))|_{z=\hat{z}} = \begin{bmatrix} A(\hat{\theta}) & M_t \\ 0 & I \end{bmatrix}, \quad (31)$$

$$H(\hat{z}(t)) = \frac{\partial}{\partial z} h(z(t))|_{z=\hat{z}} = [D \ 0], \quad (32)$$

$$M_t = \frac{\partial}{\partial \theta} (A(\theta)\hat{x}(t) + B(\theta)w(t))|_{\theta=\hat{\theta}}, \quad (33)$$

$$P(0) = \begin{bmatrix} P_1(0) & P_2(0) \\ P_2^T(0) & P_3(0) \end{bmatrix}. \quad (34)$$

Here,  $P_1(0)$  is the kinematics state error covariance sub-matrix which is related to trustworthiness of the input imaging data,  $P_3(0)$  is the covariance sub-matrix of material parameters  $E$  and  $\nu$  with values proportional to the expected errors in the corresponding parameter to ensure smooth convergence, and  $P_2(0)$  is the kinematics-material correlation sub-matrix with zero entries. Construction and implementation of the error covariance matrix is discussed next.

### 2.6. Construction of augmented state error covariance matrix

In our earlier implementation (Shi and Liu, 2002), the augmented state error covariance sub-matrices  $P_1(0)$  (state),  $P_2(0)$  (state-material correlation) and  $P_3(0)$  (material) are modeled as diagonal matrices with uniform entries ( $P_1(0)$  has separate uniform values for displacement data and velocity data when both are available). The motivation to construct non-uniform  $P_1(0)$  sub-matrix comes from the observation that the filter performance is very sensitive to the initial values. Because of the periodic nature of the cardiac dynamics, we cyclically feed the updated imaging and imaging-derived data into the filtering framework until reaching convergence. Casual and improper selections of the initial values often *destroy* the integrity of the finite element mesh during the filtering process. Further, we believe that any prior knowledge of the state and material parameters should enable us to achieve higher filtering efficiency and more robust results.

The state error covariance sub-matrix  $P_1(0)$  is expressed as  $P_1(0) = \text{diag}(P_{UU}(0), P_{UV}(0))$ . The first term on the diagonal is the variance of the displacements, and in our current in vivo experiment, it is related to confidence

measures of the shape-matched boundary point displacements. Similarly, the second term, the covariance of the velocity, is related to the confidence measures of the phase contrast velocity information from MR imaging and is characterized by the local phase coherence values (Chung et al., 2002).

2.6.1. Confidence measures on shape-matched boundary displacements

We had previously proposed a strategy for myocardial boundary motion tracking based on locating and matching differential geometric landmarks (Shi et al., 2000). Based on the hypothesis that the LV boundary contours deform as little as possible between successive temporal frames, bending energy measure is used as the matching criterion to obtain the point correspondences between contours:

$$\min_{\varphi \in \mathcal{C}} e_{\text{bend}}(\phi, \varphi) = \min_{\varphi \in \mathcal{C}} [\kappa_f(\phi) - \kappa_s(\varphi)]^2 \quad (35)$$

where  $\kappa_f(\phi)$  is the curvature for a point  $\phi$  in the first contour,  $\mathcal{C}$  the corresponding search region on the second contour, and  $\kappa_s(\varphi)$  the curvature of a candidate point  $\varphi$  within the search region. Among all the candidate points, the one at  $\xi$  which yields the smallest bending energy is chosen as the matched point, and the bending energy value indicates the goodness  $m_g(\xi) = e_{\text{bend}}(\phi, \xi)$  of the match.

Further, the bending energy measures for all other points

within the search region are also recorded as the basis to measure the uniqueness of the matching choice. Ideally, the bending energy value of the chosen point should be an outlier (much smaller value) compared to the values of the rest of the candidate points. If we denote the mean value of the bending energy measures of all the points inside the search window except the chosen point as  $\bar{e}_{\text{bend}}$  and the standard deviation as  $\sigma_{\text{bend}}$ , we define the uniqueness measure of the match as

$$m_u(\xi) = \left| \frac{e_{\text{bend}}(\phi, \xi)}{\bar{e}_{\text{bend}} - \sigma_{\text{bend}}} \right|. \quad (36)$$

Obviously for both goodness and unique measures, the smaller the values the more reliable the match. Combining these two together, we arrive at a confidence measure for the matched second contour point  $\xi$  of the first contour  $\phi$ :

$$c(\xi) = \frac{1}{k_{1,g} + k_{2,g}m_g(\xi)} \frac{1}{k_{1,u} + k_{2,u}m_u(\xi)}, \quad (37)$$

where  $k_{1,g}$ ,  $k_{2,g}$ ,  $k_{1,u}$  and  $k_{2,u}$  are normalizing constants such that the confidence measures for all point matches between contours are in the range of 0–1.

This process yields a set of shape-based, best-matched displacement vectors for each pair of contours, and each vector has an associated confidence measure. Elements of

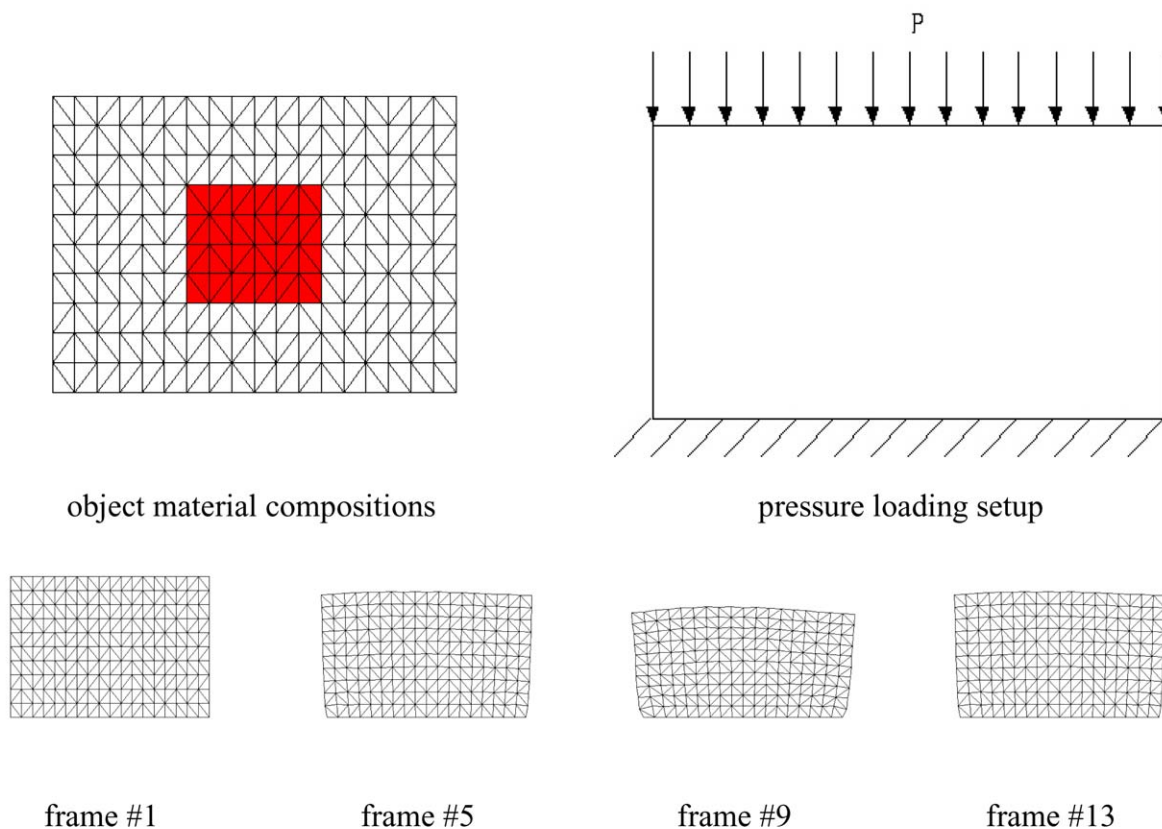


Fig. 1. Generation of the 16-frame synthetic data sequence: object material compositions and pressure loading setup (upper row), and the selected resulting meshes at frames #1, #5, #9 and #13 (lower row). (This figure is available in colour, see the on-line version.)

the displacement error covariance sub-matrix  $P_{UU}(0)$  is now weighted by  $(1 - c(\xi))$ .

2.6.2. Confidence measures on mid-wall MR phase contrast velocity

Phase contrast MRI relies on the fact that a uniform motion of tissue in the presence of a magnetic field gradient produces a change in the MR signal phase that is proportional to velocity (Pelc et al., 1991). In principle, the instantaneous Euclidian velocities for the moving tissue can be easily obtained for each pixel in an image acquisition. However, because of the relatively large size of the imaging region-of-interest, current phase contrast velocity

estimates near the endocardial and epicardial boundaries are extremely noisy, and reliable motion information is only available within the mid-wall region.

Local phase coherence (LPC) (Chung et al., 2002) is used to assess the reliability of the velocity data at mid-wall. For velocity vector  $v_s$  at  $s$  and velocity vector  $v_i$  of its neighbor at  $i$ , we define the  $LPC(v_s)$  to be

$$f(v_s, v_i) = \frac{\langle v_s, v_i \rangle}{\|v_s\| \|v_i\|}, \tag{38}$$

$$LPC(v_s) = \frac{1}{16} \left[ \sum_{i=1}^8 f(v_s, v_i) + 8 \right], \tag{39}$$

where the summation is taken over the eight neighbors.

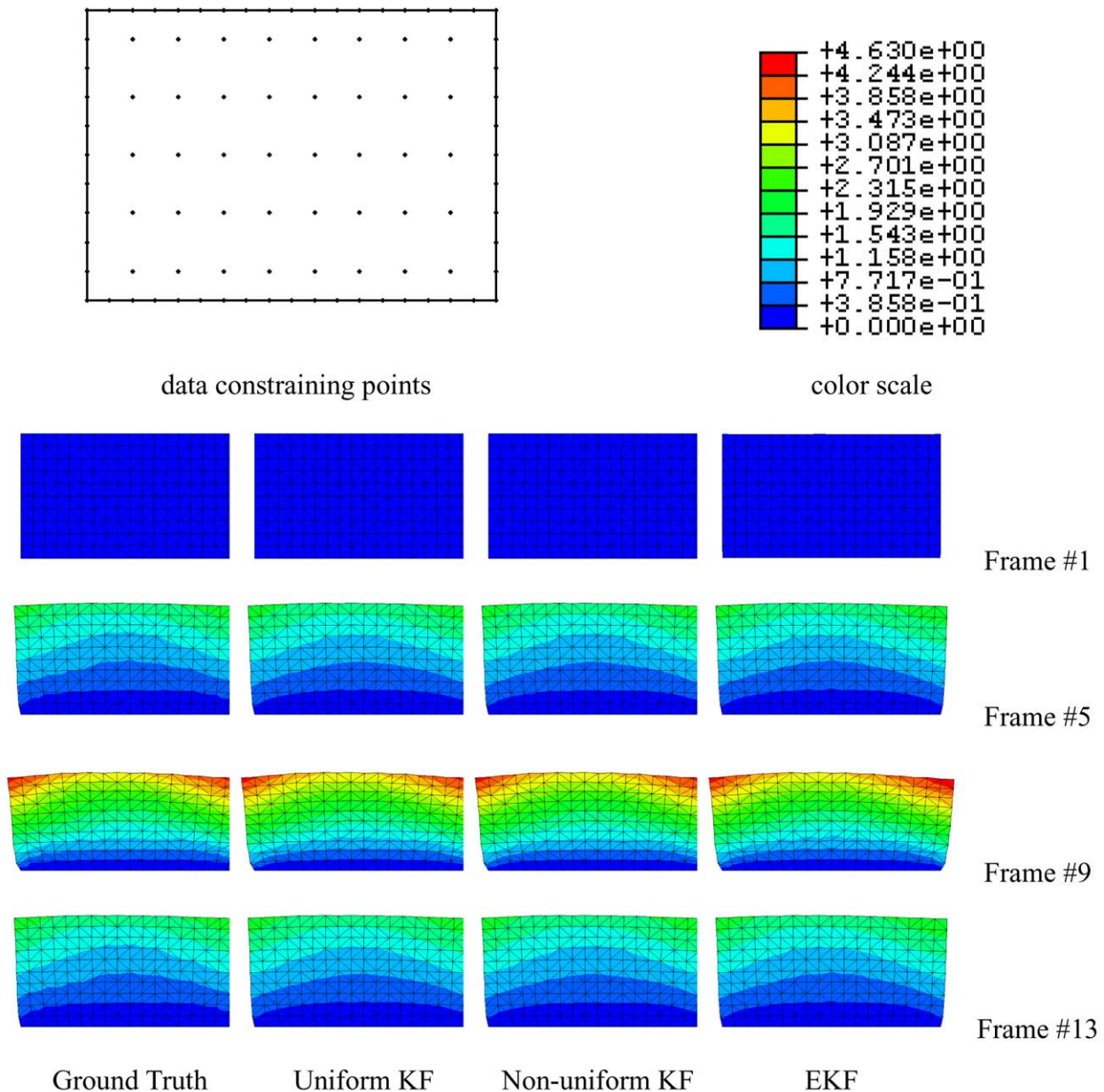
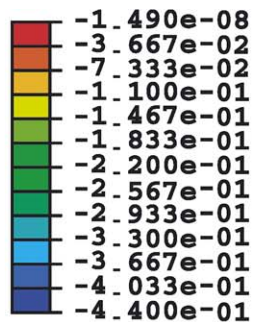
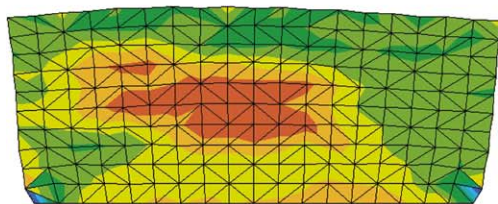


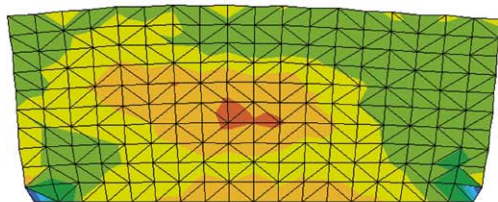
Fig. 2. Comparison of true and three estimated displacement magnitude distributions for frames #1, #5, #9 and #13. Top row shows the constraining data positions and the color scale. (This figure is available in colour, see the on-line version.)



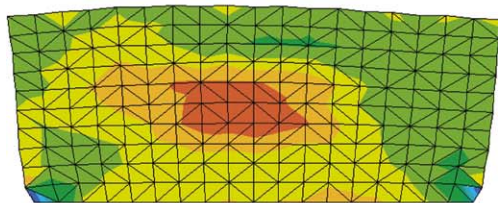
Strain Map Color Scale



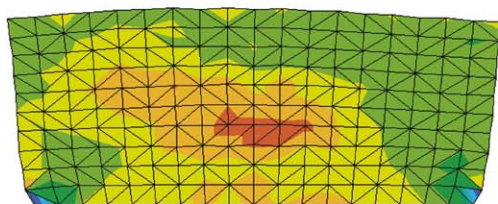
Ground Truth



Uniform KF



Non-uniform KF



EKF

Fig. 3. Comparison of true and three estimated vertical strain distributions for frame #9. Top row shows strain map color scale.

Table 1  
Kolmogorov–Smirnov hypothesis test

	Uniform	Non-uniform	EKF
H	1	0	0
P value	0.0244	0.6403	0.1038
K–S statistics	0.3429	0.1714	0.2857

Since  $f(v_s, v_i)$  is within  $[-1, 1]$ , the LPC value is thus within the range of  $[0, 1]$ .

In ideal situation, we should expect high LPC values at the velocity coherent regions of mid-wall myocardium. Any deviation from high LPC indicates poor quality of the velocity information. Elements of the velocity error covariance sub-matrix  $P_{\hat{U}\hat{U}}(0)$  now will be weighted by  $(1 - \text{LPC}(v_s))$ .

### 2.7. Other computational considerations

**Initial conditions.** Let  $i$  be the current image frame number, and  $j$  be the current filtering loop number (because the periodic nature of the cardiac dynamics, we can loop through the image sequence until convergence):

- If  $j = 1$  and  $i = 1$ , the initial displacements are zero. Otherwise, the initial displacements are estimated from all previous frames/loops up to the  $(i - 1)$ th frame of the  $j$ th loop.
- MR phase contrast velocity images at the  $i$ th frame, if available, provide the  $x$ - and  $y$ -components of the instantaneous velocities for the mid-wall points. For all other points, the velocity is estimated from all previous frames up to the  $(i - 1)$ th frame of the  $j$ th loop.

- The initial accelerations of all points are estimated from all previous frames up to the  $(i - 1)$ th frame of the  $j$ th loop.
- If  $j = 1$  and  $i = 1$ , the initial Young's modulus and Poisson's ratio are set to 75 000 Pa and 0.47, respectively (Yamada, 1970). Otherwise, we use the values estimated from all previous frames up to the  $(i - 1)$ th frame of the  $j$ th loop.
- The initial equivalent total loads are computed from the governing equations using all the initial conditions.

**Boundary conditions.** The system equations are modified to account for the boundary conditions of the dynamic system. If the displacement of an arbitrary nodal point is known to be  $U_b = b$ , say from MR tagging images or shape-based boundary tracking (Shi et al., 2000), the constraint  $kU_b = kb$  is added to the system governing equation, where  $k$  is a large number weighted by the confidence on the displacement. Other possible strategies to enforce boundary conditions can be found at many standard finite element books (Bathe and Wilson, 1976; Cook, 1995).

**Error measures of the estimation process.** The filtering process is optimized by minimizing a set of error residuals, based on the differences between experimentally measured imaging and image-derived data, i.e. mid-wall MR phase contrast velocity and MR tagging/shape-tracked displacement, and those estimated by EKF framework. These errors are compared to a set of thresholds to determine the convergence of the filtering process.

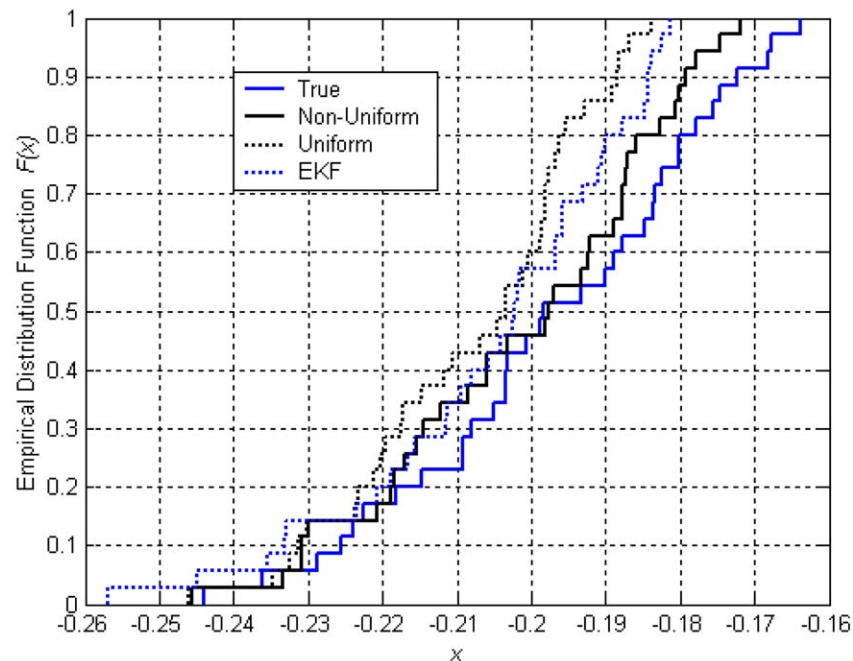


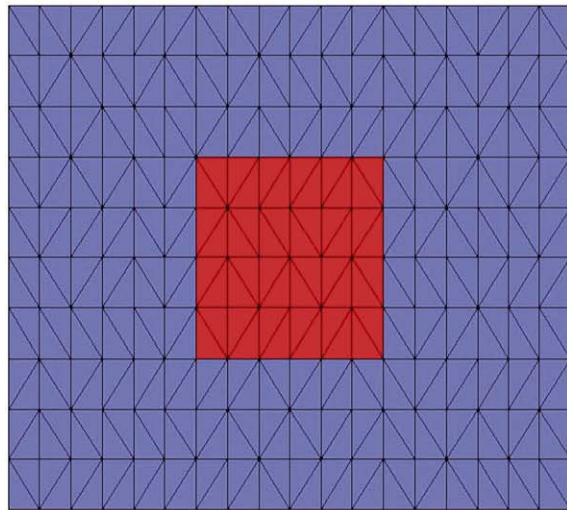
Fig. 4. Cumulative distribution functions from the Kolmogorov–Smirnov test of the true vertical strain, uniform KF strain, non-uniform strain and EKF strain. (This figure is available in colour, see the on-line version.)

### 2.8. Convergence and bias issues

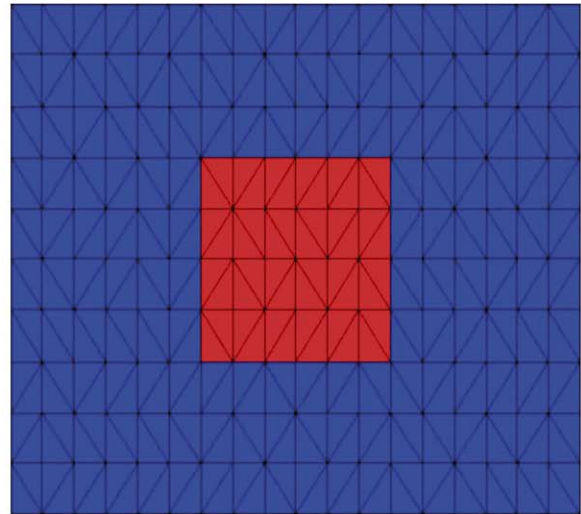
As mentioned earlier, the problem of our joint estimation of the myocardial kinematics states and material parameters is motivated from the need for a material model in order to estimate the kinematics states as in the image analysis efforts, and the need for good states estimates in order to estimate material models in biomechanics studies. The extended Kalman filter provides an efficient

method for generating *approximate* optimal estimates for the nonlinear joint estimation problem, based on first-order linearization. An essential difficulty with all approximation techniques is to establish convergence. Further, for the joint estimation results to be physiologically and clinically useful, the bias of the estimates and the convergence of the framework need to be properly addressed.

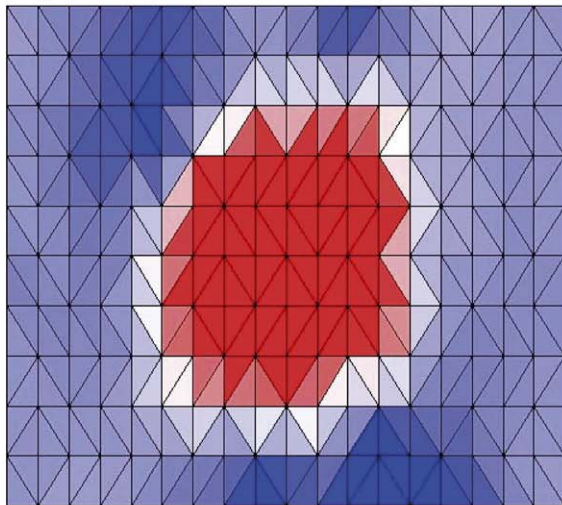
In general, the EKF estimates may be biased or divergent (Ljung, 1979). The reason for divergence can be



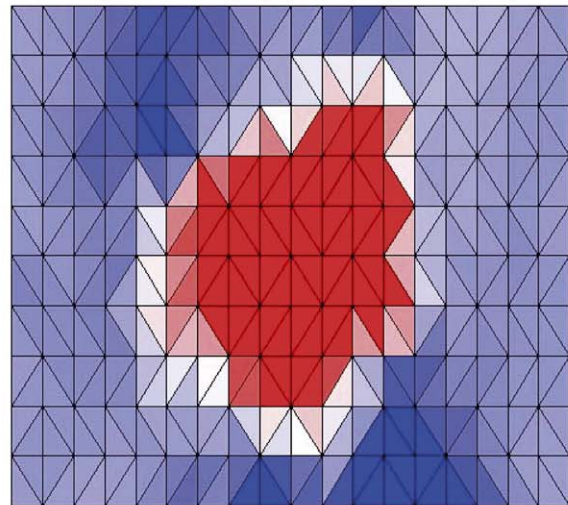
Ground Truth Young's modulus



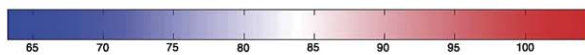
Ground Truth Poisson's ratio



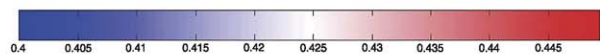
estimated Young's modulus



estimated Poisson's ratio



Young's modulus scale



Poisson's ratio scale

Fig. 5. Ground truth (top row) and EKF estimated (middle row) material parameter distributions for the synthetic data sequence.

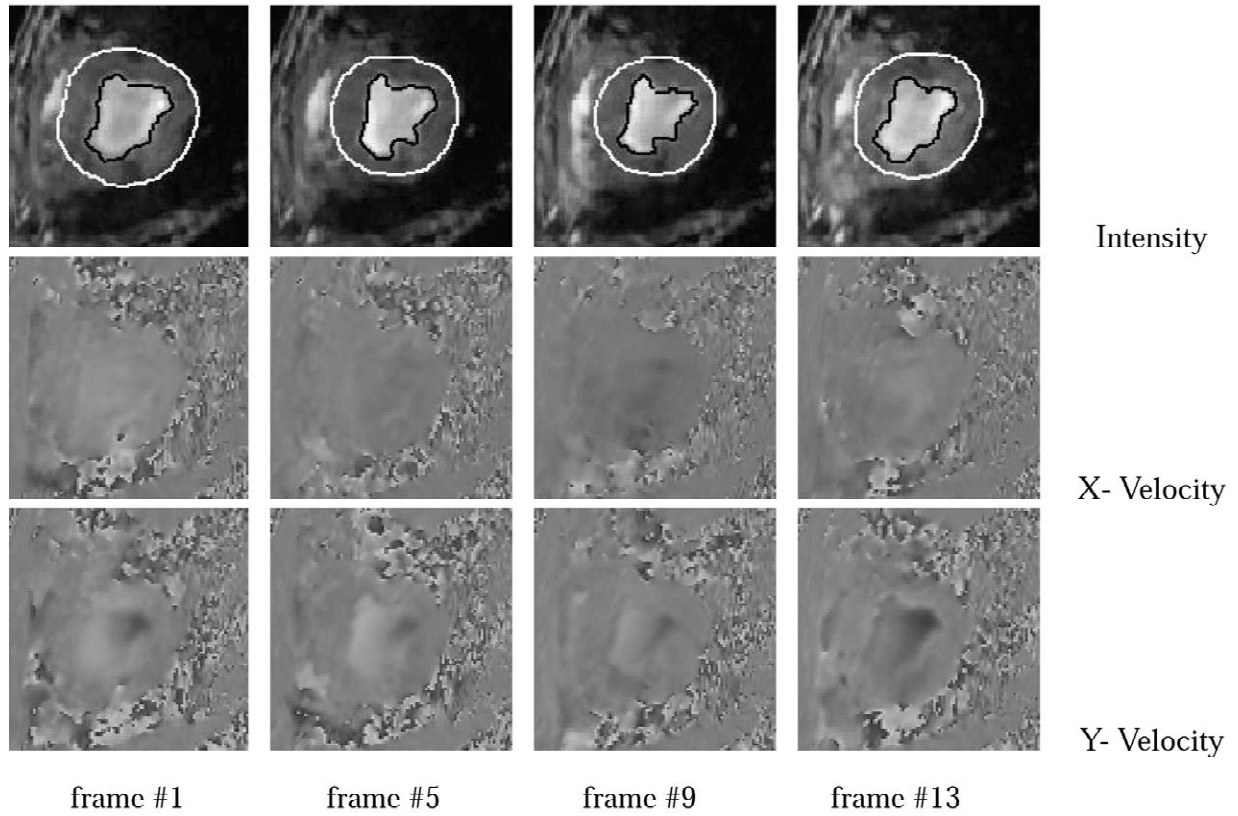


Fig. 6. Matching EEG-gated canine MR phase contrast intensity,  $x$ -velocity and  $y$ -velocity image sequences throughout cardiac cycle.

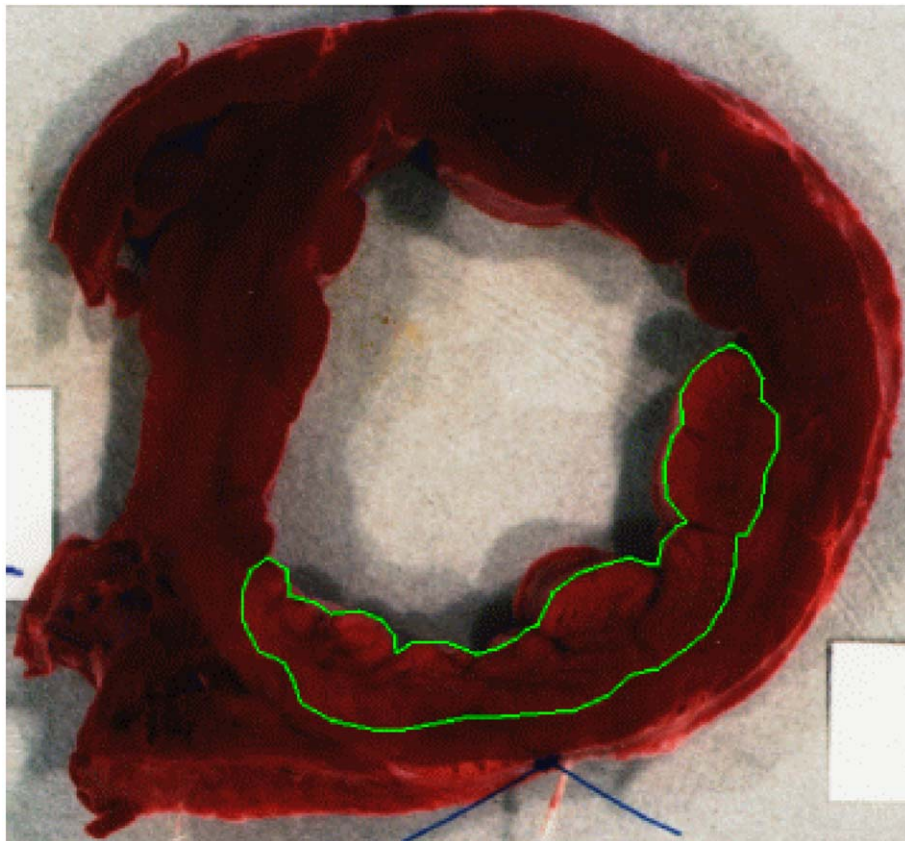


Fig. 7. TTC-stained post mortem myocardium with the infarcted tissue highlighted. (This figure is available in colour, see the on-line version.)

traced to the lack of coupling between the Kalman gain  $G(t)$  and the model parameter  $\theta$  in the algorithm. However, global convergence results can be easily obtained by modifying the coupling term  $M_t$  such that the  $i$ th column of the new term  $M_t^*$  is given by

$$M_t^{*(i)} = M_t^{(i)} + k_t^{(i)}(y(t) - D\hat{x}(t)), \quad (40)$$

where  $k_t^{(i)}$  can be derived from the so-called sensitivity equations of the EKF (Ljung, 1979). This procedure can be interpreted as a minimization of the prediction error associated with the model parameter  $\theta$ . Further, the estimated material parameter  $\hat{\theta}$  is biased unless the processes and measurement noise characteristics are completely known a priori, which is usually not going to be satisfied in real situations. However, we do want to point out that the cause of the bias does not lie in the EKF method itself, but rather comes from imperfect noises assumptions associated with the model. In normal practices, manual adjustments of the noise covariances are often used to *tune the filter*. The inclusion of the parameters associated with the Kalman gain can thus be interpreted as automatic tuning of the filter. We are also actively exploring other filtering strategies which are less sensitive to the knowledge on the noise statistics, such as the  $H_\infty$  filters and the particle filters.

**Further considerations for error covariance matrix.** Because the matrix  $P(t)$  must be symmetric and non-negative definite, special attentions should be given in its recursive updating. If round-off errors should produce an indefinite  $P(t)$  matrix at a given step, it is repaired with a *nearby* non-negative definite matrix or through  $U-D$  factorization (Glad and Ljung, 2000).

### 3. Synthetic and in vivo experiments

#### 3.1. Synthetic computational experiment

As shown in Fig. 1, for a rectangular object consisting of two distinguished parts with different materials ( $E_{\text{mid}} = 105$  and  $\nu_{\text{mid}} = 0.49$  for the middle part, and  $E = 75$  and  $\nu = 0.4$  for the rest), distributed time varying pressure  $P(k) = 58.2(1 - \cos((k-1)\pi/n))$ , where  $n = 16$  is the total number of sampling frames and  $k$  is the  $k$ th frame, is applied onto the top of the object. Sixteen sampling frames of the object geometry are acquired (Fig. 1), along with the ground truth kinematic (displacement and strain) distributions.

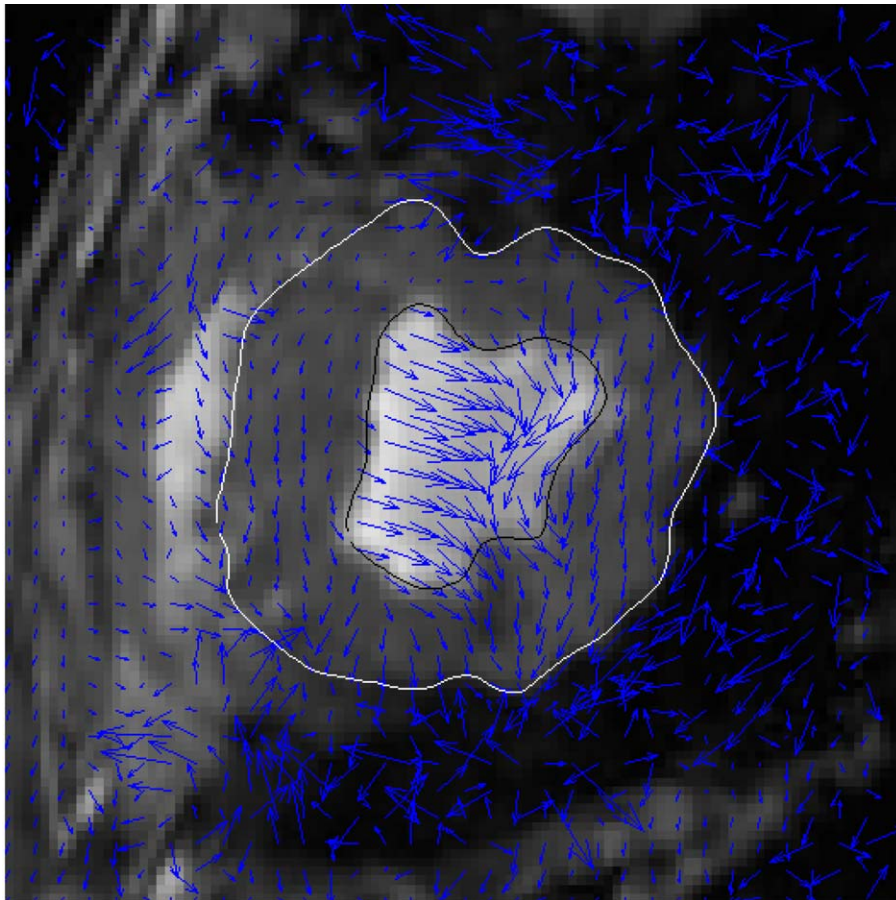


Fig. 8. Phase contrast velocity vectors (scaled for visualization purpose) overlaid on intensity image. (This figure is available in colour, see the on-line version.)

Using this set of synthetic data sequence, three types of experiments are then conducted. In the first and second experiments, the material parameters are set to be fixed constants and the goals are to recover the motion parameters using Kalman filtering (simply fixes the  $\theta$  vector in Eqs. (18) and (21)). The difference is that the first experiment uses the same uniform material values ( $E = 75, \nu = 0.4$ ) for the entire object, an almost universal practice in mechanics-based motion analysis efforts (Papademetris et al., 2002; Shi et al., 1999), while the second experiment sets the *perfect* non-uniform values for the material parameters since we are dealing with known synthetic data. In the third experiment, we use our joint extended Kalman filtering strategy to recover the material parameters and the motion parameters simultaneously.

Intuitively, since its material model parameters are exactly the same as the ones used for data generation, we expect that the Kalman filter with non-uniform model values would produce the closest results to the ground truth among the three experiments. The Kalman filter with uniform material settings would produce some errors because of the mismatch. As for the EKF, we anticipate that its results are in the middle.

For data frames #1, #5, #9 and #13, Fig. 2 shows the displacement magnitude maps of the ground truth, the KF estimated results using uniform material, the KF results using non-uniform materials and the EKF joint estimation results. With the color scale used to accommodate the range of the displacement, the experiment results are visually quite similar to each other. The more sensitive strain maps, however, exhibit the visible differences between the different experiments, as shown in Fig. 3, and the results confirm our intuition on the performance difference between the three experiments.

A detailed statistical analysis of the vertical strain distributions between the estimation results and the truth reveals a more complete story. The Kolmogorov–Smirnov test, which is suitable for comparing the distributions of values in two data vectors  $X_1$  and  $X_2$  (Zar, 1999), is adopted to compare the true vertical strain and the estimated ones. The null hypothesis for the K–S test is that  $X_1$  (truth) and  $X_2$  (estimated results) have the same distribution, and the alternative hypothesis is that they have different distributions. The result  $H$  is 1 if we can reject the hypothesis that the distributions are the same, or is 0 if we cannot reject that hypothesis. Here we reject the

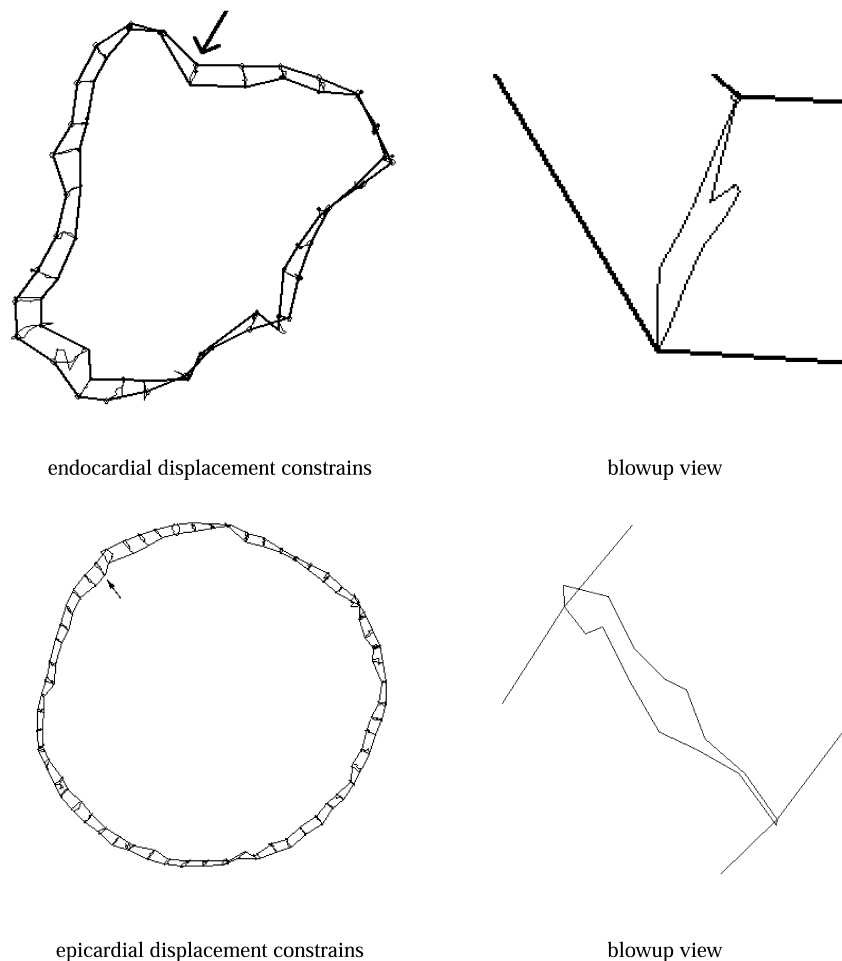


Fig. 9. Boundary displacement constraints.

hypothesis if the test is significant at the 5% level. From Table 1, we know that while the uniform KF results are not of the same distribution as the ground truth ( $p = 2.4\%$ ), we cannot make the same conclusion about the non-uniform KF and the EKF results. It is also obvious from the cumulative distribution functions (CDF) of the four

strains, as shown in Fig. 4, that the estimated results have the order of non-uniform KF, EKF, and uniform KF in terms of their closeness to the true one. The K–S statistic values, which measure the maximum differences between the CDFs, reveal the similar relationship in Table 1.

Overall, we can infer from the strain maps and the K–S

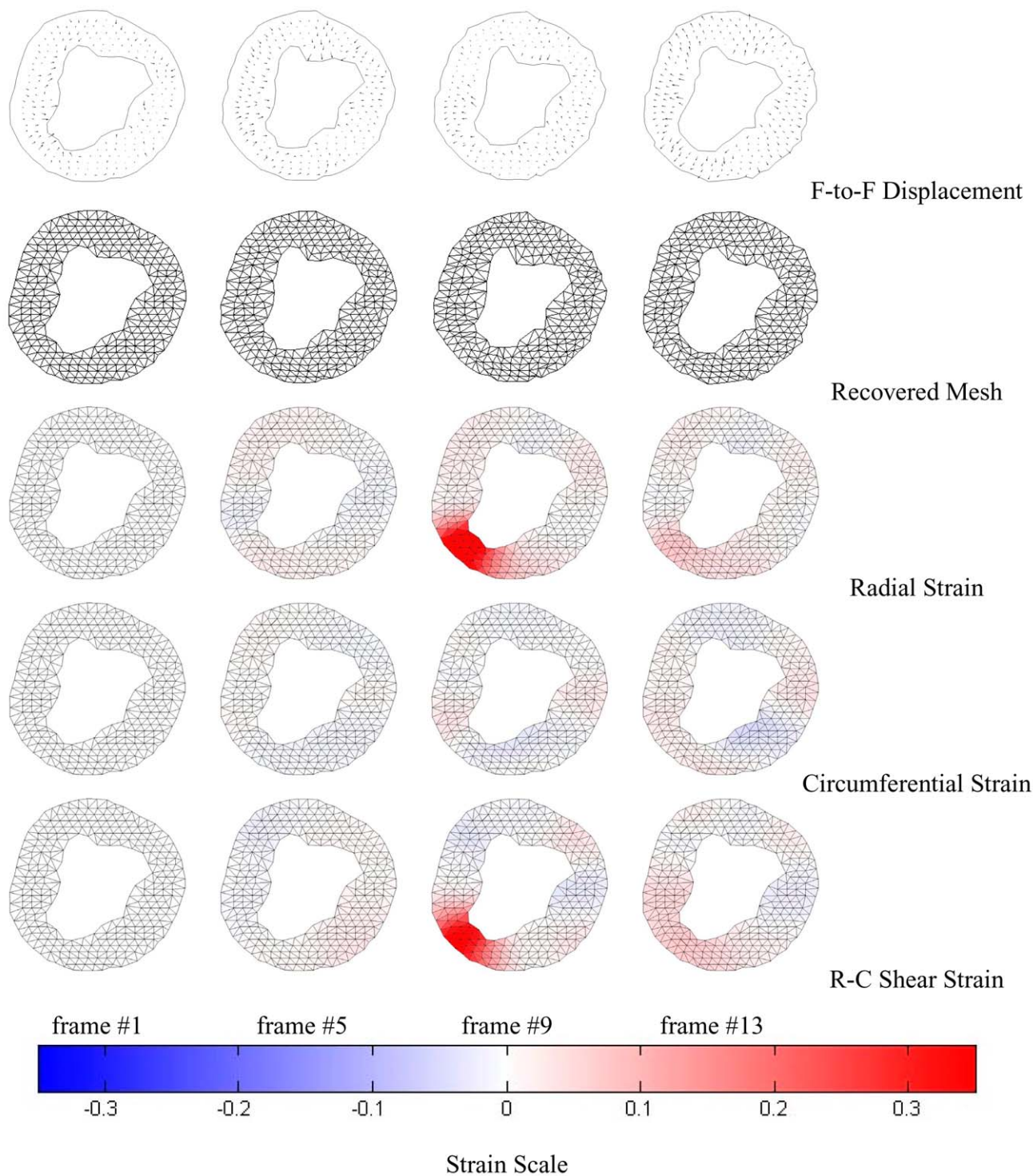


Fig. 10. With boundary displacement constraints: frame-to-frame displacement maps, deforming myocardial meshes, and cardiac-specific radial, circumferential, and R–C shear strains with respect to frame #1. (This figure is available in colour, see the on-line version.)

tests that the non-uniform Kalman filter with perfect material parameters gives the best motion estimates. In practice, however, this kind of prior knowledge is all but impossible to acquire. On the other hand, EKF does give better results than the Kalman filter with uniform materials, the typical models used in cardiac image analysis. This confirms our intentions and validates the needs for adopting a joint estimation strategy. The estimated material parameter maps are then shown in Fig. 5, compared to the ground truth material parameters used to generate the synthetic data sequence (see Fig. 1). Visually, it is quite obvious that overall the estimates from our EKF framework very closely resemble the true material properties. The errors mostly occur only at the discontinuities of the material distributions, which are actually expected since the Kalman filtering strategy is basically low-pass and it smooths out the sharp changes. Further, as pointed earlier, the material characteristics are more valuable and fundamental from physiological point of view. The good agreement between our estimates and the ground truth indicates the potential of adopting joint estimation strategy.

### 3.2. In vivo canine imaging experiment

Two kinds of canine imaging sequences are used in the experiments. The first one uses displacement constraints at

selected sampling points of myocardial boundaries. The second experiment incorporates mid-tall MRI phase contrast velocity information as well as the boundary displacement data. However, we want to point out that the joint kinematics and material analysis framework is not limited to any particular types of imaging data. Any imaging/imaging-derived data with acceleration, velocity and displacement information can be easily used in the framework without fundamental changes.

#### 3.2.1. Experiment setup and imaging data acquisition

Fasting adult mongrel dog was used for the collection of the imaging data. A proximal segment of the left anterior descending (LAD) coronary artery was dissected free for the placement of a Doppler flow probe, hydraulic and snare occluders, which enabled the production of a controlled, graded coronary stenosis.

Magnetic resonance images of a mid-ventricle short axis slice were collected using cine phase contrast gradient echo sequence for 16 time frames. The imaging parameters were: flip angle =  $30^\circ$ , TE = 34 ms, TR = 34 ms, FOV = 28 cm, 5 mm skip 0, matrix  $256 \times 128$ , 4 nex,  $v_{enc} = 15$  cm/s. The resulting spatial resolution is 1.09 mm/pixel, and the temporal resolution is 0.03125 s/frame. The intensity values of the velocity images range from  $-150$  to 150 mm/s, with the signs of the value indicating the

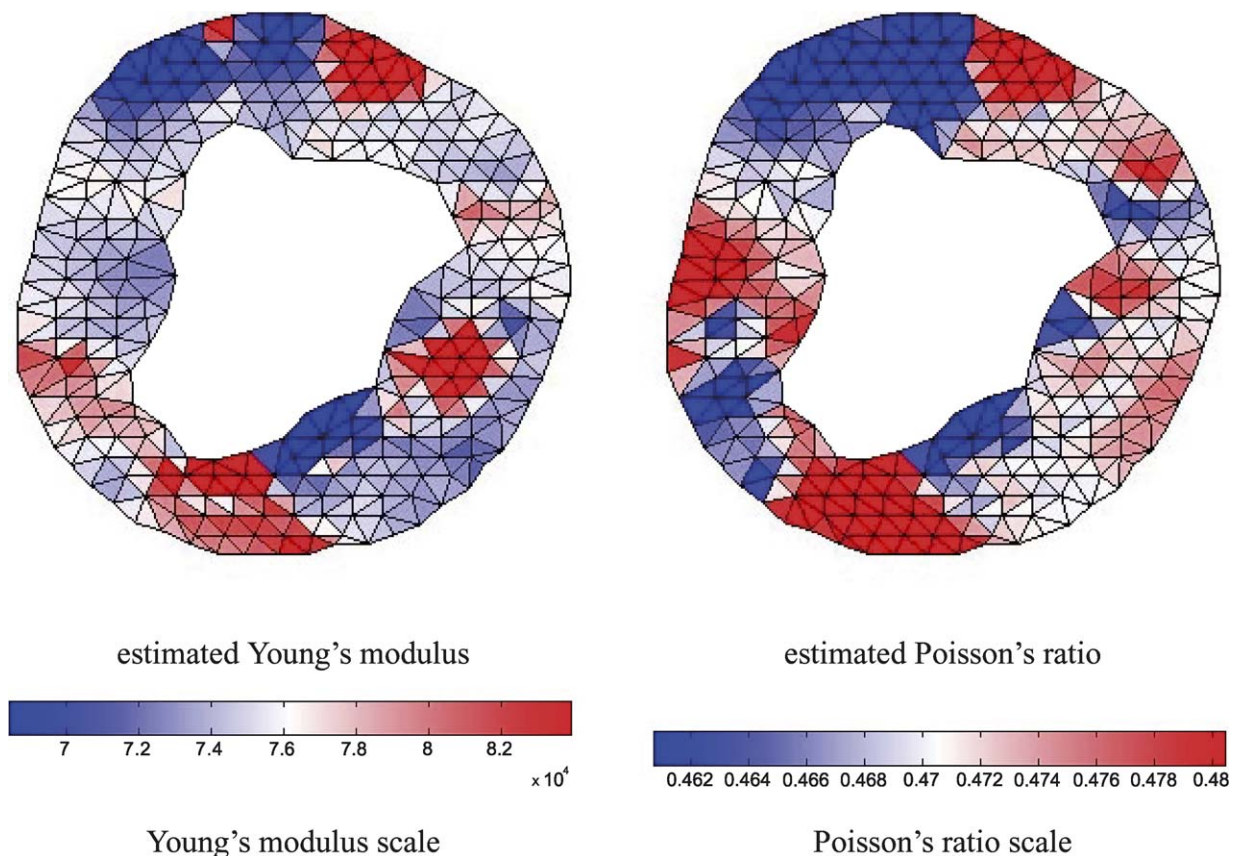


Fig. 11. Estimated material parameter distributions (boundary displacement constraints).

directions of the velocities. MR phase contrast velocity imaging relies on the fact that a uniform motion of tissue in the presence of a magnetic field gradient produces a change in the MR signal phase,  $\varphi$ , that is proportional to its velocity (Pelc et al., 1991):

$$\varphi = v\gamma M_1 = v\gamma \int_0^{TE} t G(t) dt, \tag{41}$$

where  $G(t)$  is the magnetic gradient strength (the gradient

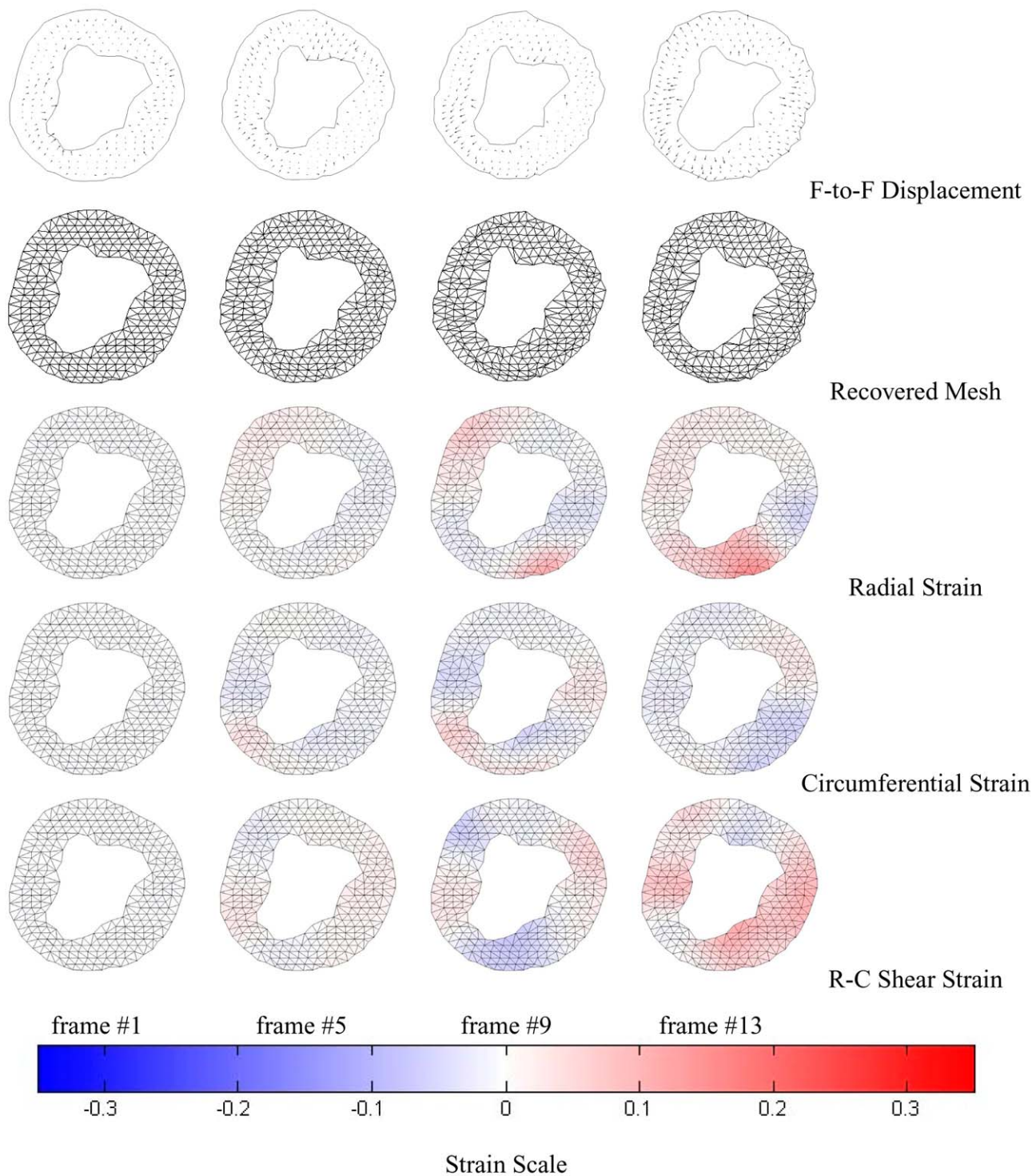


Fig. 12. With boundary displacement and mid-wall velocity constraints: frame-to-frame displacement maps, deforming myocardial meshes, and cardiac-specific radial, circumferential, and R–C shear strains with respective to frame #1. (This figure is available in colour, see the on-line version.)

waveform),  $v$  is the tissue velocity,  $M_1$  is the first moment of the gradient waveform, TE is the echo delay time, and  $\gamma$  is the gyro-magnetic ratio. The gradient waveform can be modified to alter the first moment (motion sensitivity) while maintaining the same image localization characteristics. Images acquired with this altered waveform will have a different phase shift due to motion, and the velocity in a particular spatial direction can be estimated by measuring the difference in phase shift between two acquisitions with different first gradient moments. Hence, instantaneous velocity maps encoded for motion in all three spatial dimensions may easily be obtained at multiple time instances throughout the cardiac cycle using a phase contrast cine-MR imaging sequence.

Fig. 6 shows the segmented intensity images of the ECG-gated MR sequence, as well as the matching  $x$ - and  $y$ -phase contrast velocity images over the cardiac cycle. In addition, the highlighted histological result of triphenyl tetrazolium chloride (TTC) stained post mortem mid-ventricle myocardial slice is shown in Fig. 7, where the infarcted tissue region is marked.

From the matching intensity and velocity images, shape-matched boundary displacements (Shi et al., 2000) and mid-wall phase contrast velocity are used as the data inputs in the experiments of the estimation framework. Fig. 8 shows the phase contrast velocity vectors overlaid on intensity image, and Fig. 9 shows the endocardial and

epicardial displacement constraints throughout the cardiac cycle.

### 3.2.2. Results and discussion

**With boundary displacement constraints.** The top row of Fig. 10 shows the estimated frame-to-frame displacement maps for selected myocardial frames (the magnitude of the displacement vectors are uniformly magnified for visualization purposes), while the second row presents the resulting mesh deformation throughout the cardiac cycle. Please note that since the boundary displacements have been filtered by the EKF, they are somewhat different from the original input constraining displacements. Corresponding to the highlighted infarct region of Fig. 7, there are signs of dyskinesias (impairment of voluntary movements resulting in fragmented or jerky motions) at the lower-right quarter of the myocardium. During the general contraction phase (i.e. frame #1 to #7), there are little contracting motion at the infarct zone until frame #6. At the beginning stage of the general expansion stage (frame #8 to #9), the infarcted tissues continue their contracting motion while the other tissues start to expand. The expansion at the infarct zone does not occur until frame #13. From the displacements, the cardiac-specific radial (R), circumferential (C), and R–C shear strain (with respect to frame #1) are computed, as shown in Fig. 10.

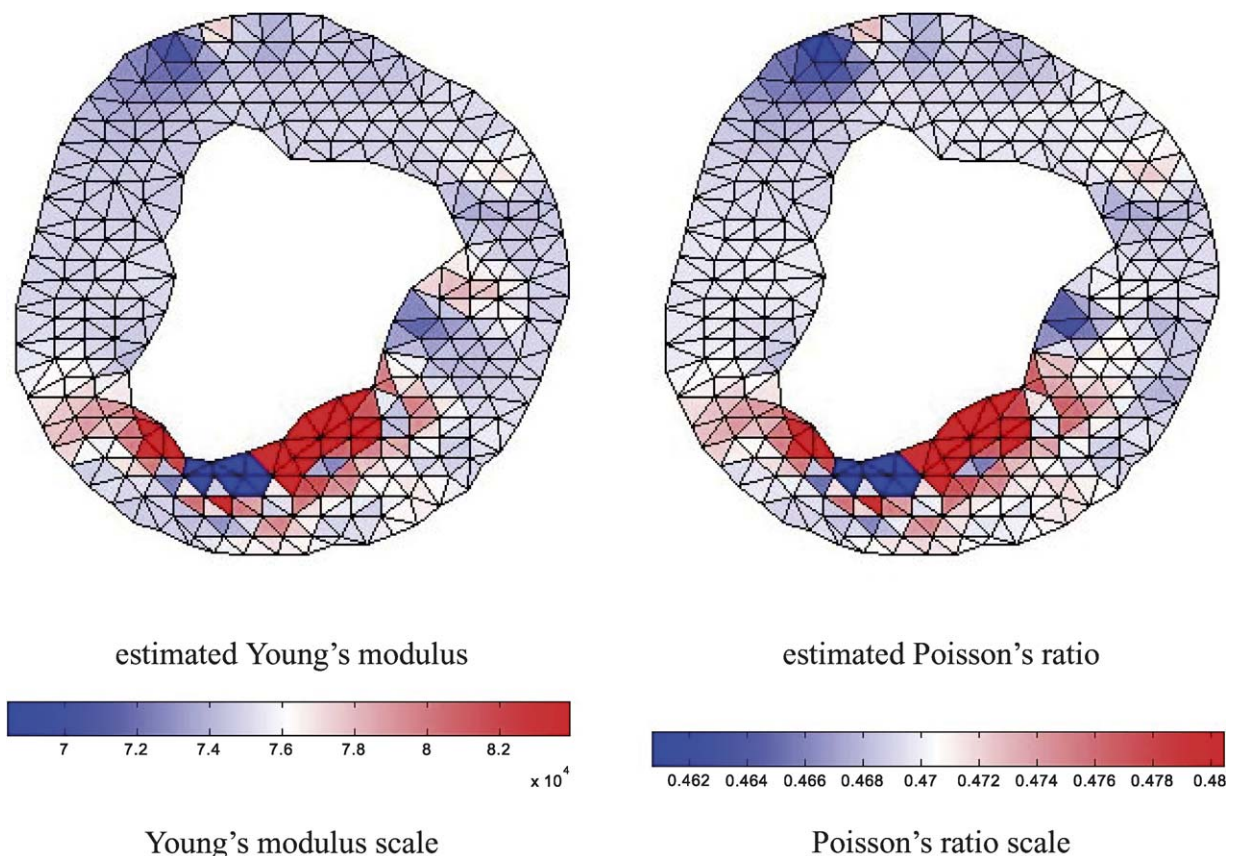


Fig. 13. Estimated material parameter distributions (boundary displacement and mid-wall velocity constraints).

However, other than the circumferential stains, the strain distributions do not exhibit obvious abnormality at the infarct region. Finally, the estimated non-uniform material parameter distributions are shown in Fig. 11. While they appear to be more sensitive than the motion parameters, the current limited results are quite difficult to be meaningfully interpreted.

**With boundary displacement and mid-wall velocity constraints.** Similarly, the top row of Fig. 12 shows the estimated frame-to-frame displacement maps for the myocardial slice, while the second row presents the mesh deformation throughout the cardiac cycle. The displacement maps show similar pattern as the previous experiment, and dyskinesias is obvious at the infarct zone once again. The radial (R), circumferential (C), and R–C shear strain maps, in contrast to the boundary constraint experiment, show significant differences at the infarct tissues. Finally, the estimated material parameter distributions are shown in Fig. 13. Here, these material maps exhibit vastly different material parameters at the infarct zone from the normal tissues, and the patterns are in very good agreement with the highlighted histological results of triphenyl tetrazolium chloride (TTC) stained post mortem myocardium (see Fig. 7), often considered the gold-standard. Further, the infarct zone myocardial tissues are relatively stiffer than normal with larger Young's modulus values, and they are more difficult to compress with larger Poisson's ratios (there is less or no blood supplied to these tissues), both of which have been observed in post mortem tissue experiments earlier.

Compared to the boundary constraint only case, the inclusion of mid-wall velocity dramatically improve the motion and material estimates results, using the TTC-staining as the guidance. This is not really surprising given the fact that the phase velocity gives transmural information of the myocardium.

#### 4. Conclusion

We have developed a biomechanically constrained stochastic finite element framework for multi-frame joint estimation of the cardiac kinematics and material properties from medical image sequence. Coupling stochastic modeling of the myocardial behavior with finite element method, this strategy deals with noisy imaging data and uncertain constraining material parameters in a coordinated effort. We believe that this is the first attempt in image analysis that incorporates uncertain constraining models in the ill-posed recovery problems. The joint estimation strategy offers new possibilities to study myocardial kinematics and material characteristic from a variety of imaging data, and canine imaging experiments with the extended Kalman filter algorithm have shown that material parameters have better sensitivity for transmural properties

than motion parameters, as validated by the TTC-stained post mortem tissues.

#### Acknowledgements

This work is supported in part by the Hong Kong Research Grant Council under grant CERG HKUST6057/00E, and by a HKUST Postdoctoral Fellowship Matching Fund. The authors would like to extend their gratitude to Dr. Albert Sinusas of Yale University for the canine experiment and imaging data. The valuable comments and suggestions from the anonymous reviewers are also greatly appreciated.

#### References

- Amini, A.A., Duncan, J.S., 1992. Bending and stretching models for LV wall motion analysis from curves and surfaces. *Image and Vision Computing* 10 (6), 418–430.
- Amini, A.A., Chen, Y.S., Elayyadi, M., Radeva, P., 2001. Tag surface reconstruction and tracking of myocardial beads from SPAMM-MRI with parametric B-spline. *IEEE Transactions on Medical Imaging* 20 (2), 94–103.
- Bar-Shalom, Y., Li, X.R., Kirubarajan, T., 2001. *Estimation with Applications to Tracking and Navigation*. Wiley, New York.
- Bathe, K., Wilson, E., 1976. In: *Numerical Methods in Finite Element Analysis*. Prentice-Hall, Englewood Cliffs, NJ.
- Benayoun, S., Ayache, N., 1998. Dense non-rigid motion estimation in sequences of medical images using differential constraints. *International Journal of Computer Vision* 26 (1), 25–40.
- Chung, A.C.S., Noble, J.A., Summers, P., 2002. Fusing speed and phase information for vascular segmentation of phase contrast MR angiograms. *Medical Image Analysis* 6, 109–128.
- Constable, R.T., Rath, K., Sinusas, A., Gore, J., 1994. Development and evaluation of tracking algorithms for cardiac wall motion analysis using phase velocity MR imaging. *Magnetic Resonance in Medicine* 32, 33–42.
- Contreras, H., 1980. The stochastic finite element method. *Computers and Structures* 12, 341–348.
- Cook, R.D., 1995. *Finite Element Modeling for Stress Analysis*. Wiley, New York.
- Creswell, L.L., Moulton, M.J., Wyers, S.G., Pirollo, J.S., Fishman, D.S., Perman, W.H., Myers, K.W., Actis, R.L., Vannier, M.W., Szabo, B.A., Pasque, M.K., 1994. An experimental method for evaluating constitutive models of myocardium in in vivo hearts. *American Journal of Physiology* 267, H853–H863.
- Denney, T.S., 1999. Estimation and detection of myocardial tags in MR image without user-defined myocardial contours. *IEEE Transactions on Medical Imaging* 18 (4), 330–344.
- Denney, T.S., Prince, J.L., 1995. Reconstruction of 3-D left ventricular motion from planar tagged cardiac MR images: an estimation theoretic approach. *IEEE Transactions on Medical Imaging* 14 (4), 625–635.
- Duncan, J.S., Ayache, N., 2000. Medical image analysis: progress over two decades and the challenges ahead. *IEEE Transactions on Pattern Analysis and Machine Intelligence* 22 (1), 85–106.
- Frangi, A.J., Niessen, W.J., Viergever, M.A., 2001. Three-dimensional modeling for functional analysis of cardiac images: A review. *IEEE Transactions on Medical Imaging* 20 (1), 2–25.
- Frangi, A.J., Rueckert, D., Duncan, J.S., 2002. Three-dimensional cardiovascular image analysis. *IEEE Transactions on Medical Imaging* 21 (9), 1005–1010.
- Geerts, L., Bovendeerd, P., Nicolay, K., Arts, T., 2002. Characterization

- of the normal cardiac myofiber field in goat measured with MR-diffusion tensor imaging. *American Journal of Physiology* 283 (1), H139–H145.
- Glad, T., Ljung, L., 2000. *Control Theory*. Taylor & Francis, London.
- Glass, L., Hunter, P., McCulloch, A., 1991. *Theory of Heart*. Springer, New York.
- Golub, G.H., Van Loan, C.F., 1983. *Matrix Computation*. Johns Hopkins University Press, Baltimore, MD.
- Guccione, J.M., McCulloch, A.D., Waldman, L.K., 1991. Passive material properties of intact ventricular myocardium determined from a cylindrical model. *Journal of Biomechanical Engineering* 113, 42–55.
- Guttman, M.A., L Prince, J., McVeigh, E.R., 1994. Tag and contour detection in tagged MR images of the left ventricle. *IEEE Transactions on Medical Imaging* 13, 74–88.
- Hu, Z., Metaxas, D., Axel, L., 2002. In vivo strain and stress estimation of the left ventricle from MRI images. In: *Medical Image Computing and Computer Assisted Intervention*, pp. 706–713.
- Huang, J., Abendschein, D., Davila-Roman, V.G., Amini, A.A., 1999. Spatio-temporal tracking of myocardial deformations with a 4-D B-spline model from tagged MRI. *IEEE Transactions on Medical Imaging* 18 (10), 957–972.
- Hunter, P.J., Smaill, B.H., 1989. The analysis of cardiac function: a continuum approach. *Progress in Biophysics and Molecular Biology* 52, 101–164.
- Ikeda, N., 1996. *Ito's Stochastic Calculus and Probability Theory*. Springer, Tokyo.
- Kambhamettu, C., Goldgof, D.B., 1994. Curvature-based approach to point correspondence recovery in conformal nonrigid motion. *CVGIP: Image Understanding* 60 (1), 26–43.
- Kerwin, W.S., Prince, J.L., 1999a. The kriging update model and recursive space-time function estimation. *IEEE Transactions on Signal Processing* 47 (11), 2942–2952.
- Kerwin, W.S., Prince, J.L., 1999b. Tracking MR tag surfaces using a spatiotemporal filter and interpolator. *International Journal of Image System and Technology* 10 (2), 128–142.
- Klieber, M., Tran, D.H., 1992. *The Stochastic Finite Element Method: Basic Perturbation Technique and Computer Implementation*. Wiley, Chichester.
- Kumar, S., Goldgof, D., 1994. Automatic tracking of SPAMM grid and the estimation of deformation parameters from cardiac MR images. *IEEE Transactions on Medical Imaging* 13 (1), 122–132.
- Lipton, M.J., Bogaert, J., Boxt, L.M., Reba, R.C., 2002. Imaging of ischemic heart disease. *European Radiology* 12, 1061–1080.
- Liu, W.K., Belytschko, T., Man, A., 1986. Random field finite element. *International Journal for Numerical Methods in Engineering* 23, 1831–1845.
- Ljung, L., 1979. Asymptotic behavior of the extended kalman filter as a parameter estimator for linear systems. *IEEE Transactions on Automatic Control* 21 (1), 36–50.
- Manduca, A., Oliphant, T.E., Dresner, M.A., Mahowald, J.L., Kruse, S.A., Amromin, E., Felmlee, J.P., Greenleaf, J.F., Ehman, R.L., 2001. Magnetic resonance elastography: non-invasive mappings of tissue elasticity. *Medical Image Analysis* 5, 237–254.
- McCulloch, A.D., 1995. Cardiac mechanics. In: *The Biomedical Engineering Handbook*. CRC Press, Boca Raton, FL, pp. 418–439.
- McEachen, J.C., Duncan, J.S., 1997. Shape-based tracking of left ventricular wall motion. *IEEE Transactions on Medical Imaging* 16 (3), 270–283.
- McEachen, J.C., Nehorai, A., Duncan, J.S., 2000. Multiframe temporal estimation of cardiac nonrigid motion. *IEEE Transactions on Image Processing* 9, 651–665.
- Meyer, F.G., Constable, R.T., Sinusas, A.J., Duncan, J.S., 1996. Tracking myocardial deformation using spatially constrained velocities. *IEEE Transactions on Medical Imaging* 15 (4), 453–465.
- Moore, C.C., O'Dell, W.G., McVeigh, E.R., Zerhouni, E.A., 1992. Calculation of three-dimensional left ventricular strains from bi-planar tagged MR images. *Journal of Magnetic Resonance Imaging* 2, 165–175.
- Moulton, M.J., Creswell, J.J., Actis, R.L., Myers, K.W., Vannier, M.W., Szabo, B.A., Pasque, M.K., 1995. An inverse approach to determining myocardial material properties. *Journal of Biomechanics* 28 (8), 935–948.
- Muthupilla, R., Lomas, D.J., Rossman, P.J., Greenleaf, J.F., Manduca, A., Ehman, R.L., 1995. Magnetic resonance elastography by direct visualization of propagating acoustic strain waves. *Science* 269 (5232), 1854–1857.
- Nielsen, P.M., LeGrice, I.J., Smaill, B.H., Hunter, P.J., 1991. Mathematical model of geometry and fibrous structure of the heart. *American Journal of Physiology* 260 (4), H1365–H1378.
- Osman, N.F., McVeigh, E.R., Prince, J.L., 2000. Imaging heart motion using harmonic phase MRI. *IEEE Transactions on Medical Imaging* 19 (3), 186–202.
- Papademetris, X., Sinusas, A.J., Dione, D.P., Duncan, J.S., 2001. Estimation of 3D left ventricular deformation from echocardiography. *Medical Image Analysis* 5, 17–28.
- Papademetris, X., Sinusas, A.J., Dione, D.P., Constable, R.T., Duncan, J.S., 2002. Estimation of 3-D left ventricular deformation from medical images using biomechanical models. *IEEE Transactions on Medical Imaging* 21 (7), 786–799.
- Park, J., Metaxas, D.N., Axel, L., 1996. Analysis of left ventricular wall motion based on volumetric deformable models and MRI-SPAMM. *Medical Image Analysis* 1, 53–71.
- Pelc, N.J., Herfkens, R.J., Shimakawa, A., Enzmann, D., 1991. Phase contrast cine magnetic resonance imaging. *Magnetic Resonance Quarterly* 7 (4), 229–254.
- Pelc, N.J., Drangova, M., Pelc, L.R., Zhu, Y., Noll, D., Bowman, B., Herfkens, R.J., 1995. Tracking of cyclical motion using phase contrast cine MRI velocity data. *Journal of Magnetic Resonance Imaging* 5, 339–345.
- Sciaroff, S., Pentland, A.P., 1995. Modal matching for correspondence and recognition. *IEEE Transactions on Pattern Analysis and Machine Intelligence* 17 (6), 545–561.
- Shi, P., Liu, H., 2002. Stochastic finite element framework for cardiac kinematics function and material property analysis. In: *Medical Image Computing and Computer Assisted Intervention*, pp. 634–641.
- Shi, P., Sinusas, A., Constable, R.T., Duncan, J., 1999. Volumetric deformation analysis using mechanics-based data fusion: Applications in cardiac motion recovery. *International Journal of Computer Vision* 35 (1), 87–107.
- Shi, P., Sinusas, A., Constable, R.T., Ritman, E., Duncan, J., 2000. Point-tracked quantitative analysis of left ventricular motion from 3D image sequences. *IEEE Transactions on Medical Imaging* 19 (1), 36–50.
- Waldman, L.K., Fung, Y.C., Covell, J.W., 1985. Transmural myocardial deformation in the canine left ventricle: normal in vivo three-dimensional finite strains. *Circulation Research* 57, 152–163.
- Wickline, S.A., Verdonk, E.D., Wong, A.K., Shepard, R.K., Miller, J.G., 1992. Structural remodelling of human myocardial tissue after infarction: quantification with ultrasonic backscatter. *Circulation* 85, 269–278.
- Wong, A.L.N., Liu, H., Shi, P., 2002. Velocity field constrained front propagation for segmentation of cardiac images. In: *IEEE Workshop on Applications of Computer Vision* (in press).
- Yamada, H., 1970. *Strength of Biological Material*. Williams & Wilkins, Baltimore, MD.
- Young, A.A., Kraitchman, D.L., Dougherty, L., Axel, L., 1995. Tracking and finite element analysis of stripe deformation in magnetic resonance tagging. *IEEE Transactions on Medical Imaging* 14 (3), 413–421.
- Zar, J.H., 1999. *Biostatistical Analysis*. Prentice-Hall, Upper Saddle River, NJ.
- Zhu, Y., Pelc, N.J., 1999. A spatiotemporal model of cyclic kinematics and its application to analyzing nonrigid motion with MR velocity images. *IEEE Transactions on Medical Imaging* 18 (7), 557–569.
- Zhu, Y., Drangova, M., Pelc, N.J., 1997. Estimation of deformation gradient and strain from Cine-PC velocity data. *IEEE Transactions on Medical Imaging* 16 (6), 840–851.